This is a preproof accepted article for *Journal of Glaciology*
This version may be subject to change during the production process
DOI: 10.1017/jog.2025.10081

Three-dimensional multitrack electrical conductivity method for interpretation of complex ice core stratigraphy

Liam Kirkpatrick[1], Austin Carter[2], Julia Marks-Peterson[3], Sarah Shackleton[4], T.J. Fudge[1]

1. Department of Earth and Space Sciences, University of Washington
2. Scripps Institution of Oceanography, University of California San Diego
3. College of Earth, Ocean, and Atmospheric Sciences, Oregon State University
4. Woods Hole Oceanographic Institution

Correspondence: liamkp@uw.edu

ABSTRACT

Recent ice cores from the Allan Hills, a blue ice area in Antarctica, are nearly 3 million years old. These cores extend ice core chronologies, enabling new insight into key climate periods such as the Mid-Pleistocene Transition. The interpretation of these climate records is complex because of the disturbed stratigraphy in this ice. Here we present a new three-dimensional multitrack electrical conductivity measurement method (3D ECM) to resolve layer structure. We demonstrate this technique on a cumulative 60 m of two large-diameter (241 mm) ice cores, ALHIC2201 and ALHIC2302. Measurements were taken on the upper section of both cores due to better ice core quality in this shallow ice. We find well-defined and dipping layering in both cores, averaging 29° in ALHIC2201 and 69° in ALHIC2302 from horizontal. We observe a slight, but statistically significant, decrease in dip with depth in both cores. We discuss how this new method can be applied to enable accurate, high-resolution multi-proxy record development even in ice cores with steeply dipping layers. 3D ECM improves interpretation of blue ice area cores by providing accurate, non-destructive constraints on stratigraphy.

1. INTRODUCTION

Extending ice core records beyond the 800,000-year EPICA Dome C record is the goal of multiple current and future ice coring efforts (Wolff and others, 2006; Fischer and others, 2013; Karlsson and others, 2018). Longer ice core records will provide insight into the evolution of atmospheric composition during previous climate periods such as the Mid-Pleistocene Transition (Wolff and others, 2006). Drilling in blue ice areas has emerged as a promising approach for recovering old ice at shallow depth (Spaulding and others, 2013; Higgins and others, 2015; Yan and others, 2019). Large-diameter drills can be used to obtain large sample volumes, which aids in the development of paleoclimate records in regions of highly thinned ice. The development of a dating method involving the steady increase of atmospheric ^{40}Ar over time (Bender and others, 2008) has enabled absolute age measurements of ice. Applied at the Allan Hills, this dating method has revealed a complex age-depth relationship where pockets of older and younger ice are interspersed (Higgins and others, 2015; Yan and others, 2019). The interpretation of climate records is challenging due to the complex ice flow at the site.

Understanding the complex stratigraphy of the Allan Hills cores is critical to developing accurate, high-resolution climate records. Steeply dipping layering might result in significant age offsets across the width of the core, and folding might cause discontinuities and age reversals.

This is an Open Access article, distributed under the terms of the Creative Commons Attribution licence (http://creativecommons.org/licenses/by/4.0), which permits unrestricted re- use, distribution and reproduction, provided the original article is properly cited.

https://doi.org/10.1017/jog.2025.10081 Published online by Cambridge University Press

Thus, to combine multiple proxies sampled independently on a common depth scale, it is necessary to develop a high-resolution picture of layer orientations within the ice core.

There has been a variety of efforts to image layering and stratigraphy within ice cores. Visual observation (Alley and others, 1997) and optical imaging (Svensson and others, 2005; Faria and others, 2010) have been applied to assess layer stratigraphy. Line scanners (Faria and others, 2010; Jansen and others, 2016; Svensson and others, 2005; Takata and others, 2004) enable similar data to be collected efficiently over longer sections of core. These methods provide useful observations of layer structure yet are limited to two dimensions and have the best quality in clathrate ice. In clathrate ice, gas molecules are trapped within the ice lattice rather than in bubbles, and so there are not bubbles to interfere with imaging methods. Recent work has demonstrated the potential to combine optical imaging with borehole instrumentation and assumptions about layer orientation to reconstruct ice core azimuth (Westhoff and others, 2021).

Electrical Conductivity Measurements (ECM) are a well-established measurement which is often a standard step in ice core processing (Hammer, 1980; Taylor and others, 1993, 1997; Wolff, 2000). The method has been applied in both Greenland and Antarctica to count annual layers in cores, for use in timescale development (WAIS Divide Project Members, 2013; Meese and others, 1997; Rasmussen and others, 2006; Taylor and others, 1993, 1997). ECM can also be used to identify acidity peaks from volcanic eruptions, which contribute to timescale development by providing tie points to other chronologies (Rasmussen and others, 2013; Severi and others, 2012). ECM has previously been applied to identify stratigraphy in two dimensions (Taylor and Alley, 2004; Fudge and others, 2016). Direct current (DC) is typically used in ECM devices, but alternating current (AC) is also applied in some systems (Sugiyama and others, 2000; Taylor and others, 2004). AC-ECM is a similar measurement to di-electric profiling (DEP, e.g. Moore and Paren, 1987; Wilhelms and others, 1998; Wilhelms, 2005; Mojtabavi and others, 2020) except that the electrodes are in contact with the ice rather than surrounding it. An advantage of AC-ECM is increased spatial resolution, while a disadvantage is that a quantitative measurement of the electrical properties of the ice is difficult to achieve given difficulties in quantifying electrode contact.

Multitrack ECM, which measures along parallel tracks, initially enabled stacking to reduce noise (Fudge and others, 2013; Taylor & Alley, 2004; Wolff and others, 1999). Taylor and Alley (2004) followed by Fudge and others (2016) demonstrated that parallel tracks could also be used to determine the orientation of layering across the width of the measured surface. However, this two-dimensional approach was only able to ascertain the apparent dip of observed layering, rather than the true three-dimensional orientation of layers. In this paper, we present a new method to apply multitrack ECM to constrain layering in three dimensions.

2. METHODS

2.1 ALHIC2201 and ALHIC2302 ice cores

We present three-dimensional multitrack ECM (3D ECM) data from the upper sections of two new ice cores from the Allan Hills in Victoria Land, East Antarctica. The location of the ALHIC2201 (76.73203°S, 159.35955°E, 1,993 m) and ALHIC2302 (76.74543°S, 159.37513°E, 1995 m) cores are shown in Fig. 1. Accurate dating from both cores is ongoing, though context from other cores in this area suggests the upper 50 m of these cores is hundreds of thousands of years old (Higgins and others, 2015; Yan and others, 2019). Both sites were selected to

https://doi.org/10.1017/jog.2025.10081 Published online by Cambridge University Press

accompany existing cores (ALHIC1901 and ALHIC1902). ALHIC2201 and ALHIC2302 were both drilled with the Blue Ice Drill (BID), which provides uniquely large 241 mm (~9.5”) diameter cores (Kuhl and others, 2014). Ice velocities at the drill sites are unknown but work by Spaulding and others (2012) shows velocities as high as ~0.5 m yr^{-1} in the main ice stream, reducing to mere centimeters per year approaching bedrock features (Fig. 1).

Core quality in the upper 50 m of these cores is consistently high, with continuous ~1 m sections of ice. There is evidence of fine fracturing in the upper ~10 m of both cores, possibly from thermal expansion/contraction in the shallowest ice. These fractures impacted ECM measurement in the upper 10 m of ALHIC2201; therefore, we assumed ALHIC2302 would be similarly impacted and did not complete ECM measurements on the upper 8.5 m of that core. To reduce transport logistics, these cores were cut in the field. Fig. 2 shows the cut plan for the upper sections of both cores, along with the location of ECM measurements. 3D ECM measurements were completed from 0 to 22.8 m depth in ALHIC2201, and from 8.5 to 46.4 m depth in ALHIC2302.

An orientation line is used to maintain consistent ice core azimuth across adjacent core sections where possible. Prior to drilling, an initial marking was made on the ice surface, and the corresponding azimuth was measured relative to true north. This marking was then extended onto the core as follows: The first ice core section was placed within a core tray and the core handlers drew a straight line from the initial marking along the length of the core, using the edge of the tray as a guide. As each subsequent core section was recovered, handlers aligned the bottom of the previous section with the top of the new section to maintain orientation, then extended the orientation line along the length of the new core section. The position of this mark is shown in Fig. 2. Where it is impossible to align adjacent core sections, most often due to fractured ice, core handlers note that the orientation of the line was lost. While it is possible that the orientation line may not have been drawn exactly parallel to the edge of the core tray along the vertical axis of the core, the relatively short depth spans where the orientation line was maintained (never more than 17 m) mean this source of error is unlikely to accumulate into large drifts in the orientation line. The compass azimuth of the orientation line was measured at the surface of ALHIC2201 with a handheld GPS unit, and is maintained through a depth of 17 m, which means the azimuth of the upper 17 m of this core is known. The azimuth of the ALHIC2302 orientation line was not measured.

Figure 1 somewhere near here.

2.2 3D ECM instrument

We have updated the ECM instrument to be compatible with large-diameter ice cores. The fundamental elements of this instrument were described by Taylor and others (1997) and Taylor and Alley (2004). The system can support DC-ECM and AC-ECM. The DC-ECM electrodes each have an area of 6 mm^2, while the AC-ECM system uses a larger pair of electrodes with an area of 25 mm^2. Both pairs of electrodes are separated by 10 mm. DC-ECM uses a constant 1000 V DC potential difference between the electrodes. The AC-ECM system uses a 2 V potential difference at 100 kHz frequency. Cores are moved from the storage room (at -36 °C) to the exam room (at -24°C) at least 14 hours prior to ECM measurement to ensure consistent temperature conditions. This study primarily uses the AC-ECM data because the larger electrodes result in less noise being introduced by the large bubbles in these relatively shallow ice cores.

Figure 2 somewhere near here.

https://doi.org/10.1017/jog.2025.10081 Published online by Cambridge University Press

Hardware and software improvements to the ECM system enable 3D ECM on large-diameter cores. The instrument now facilitates mm-accurate positioning in the cross-track dimension as well as the depth dimension, enabling alignment of perpendicular faces in three-dimensional space. The measurement process is to first measure one face in both AC and DC, and then rotate the ice 90° and measure a perpendicular face, as shown in Fig. 2. Completing 1 m of AC and DC 3D ECM on a quarter section of a 241 mm diameter core at 15 mm track separation takes approximately one hour with a single operator. Between 25 to 30 m of high-quality core can be measured in a week. The increase in time per core relative to previous ECM techniques is due to the following: 1) measuring wider cores; 2) increased setup time to get 3D positioning; and 3) repositioning each core between measurement of each face. An example of the resulting 3D ECM data is shown in Fig. 3. The large diameter BID ice cores help accommodate the perpendicular faces necessary for 3D ECM; applying 3D ECM on standard ~4" cores would require careful cut plans to provide two perpendicular faces of enough width to resolve layering.

Figure 3 somewhere near here.

2.3 Three-dimensional orientation calculation

After two-dimensional multitrack AC-ECM data has been collected on two perpendicular faces, it is possible to calculate the dip and dip direction. We use the following terminology:

- *Apparent dip*: the inclination of observed layering as seen in a single plane, which must be less than or equal to the dip.
- *Dip*: the inclination of observed layering from the horizontal plane (between 0° and 90°).
- *Dip direction*: the direction of steepest descent relative to an orientation line drawn on the core (between 0° and 360°). Note that this is distinct from the azimuth of the dip direction.
- *Azimuth*: the direction relative to true north. The azimuth of the orientation line is measured, which enables the calculation of the azimuth of the dip direction, as described in the Results section of this paper.

Figure 4 somewhere near here.

The method described below assumes that layer orientations are consistent for the full core section (roughly 1 m in length). It does not attempt to resolve cm-scale folding or disturbances to layering, although a visual evaluation of the data indicates these are not present. We calculate the dip and dip direction from 3D ECM data as follows:

1. *Clean data***:** First, we manually process the 3D ECM data, removing sections flagged for poor ice quality or surface defects. We ignore the upper and lower 10 mm of each track as the core ends introduce noise. We also apply a running 10 mm median smoothing.
2. *Compute apparent dip on a single face (δ_1):* We calculate an apparent dip for every pair of tracks on a given face by adjusting the depth of a pair of tracks until the correlation between them is maximized. This depth adjustment is used to calculate an apparent dip given the horizontal spacing of the two tracks. In an ideal case, with six tracks per face, there are a total of 15 pairs to test. Notably, cut geometry does limit this to as little as three tracks per face on some sections of ALHIC2201. Electrode contact issues also mean the data from some tracks is unusable.

   For each pair of tracks, we identify the longest section of overlap between tracks maintained across the full range of dips to be considered (-75° to 75°). Any length of

https://doi.org/10.1017/jog.2025.10081 Published online by Cambridge University Press

surface defects on the core noted during data collection is also excluded from the overlap. We do not compute a dip for any pair of tracks where this overlap is shorter than 20 cm.

At each angle from -75° to 75°, at 0.1° increments, we shift the depth record for each track by the track's distance from the center of the core multiplied by the tangent of the angle. Two tracks, before and after this depth shift, can be seen in Fig. 4c. Each track is then interpolated onto a common 1 mm depth vector, and a Pearson correlation coefficient for the pair of tracks is calculated. The results of this calculation for one core section are shown in Fig. 4d. The angle with the largest correlation coefficient is then taken as δ_1, the apparent dip for this pair of tracks. The angle δ_1, the length of the overlap, and the associated correlation coefficient are recorded.

3. *Compute apparent dip on the perpendicular face (δ_2):* We repeat the same process as above on the perpendicular face from the same core section to find δ_2, the second apparent dip.
4. *Compute dip direction (α):* With two sets of apparent dip (δ_1 and δ_2) on perpendicular faces, we can determine the 3D orientation of the layering. This is performed for every combination of angle picks from the two faces, which with 15 picks on each face results in 15^2=225 total dip estimates (for ideal core sections). If there are less than 3 apparent dip estimates on a given face due to cut geometry or electrode contact issues, we do not proceed with computing a dip direction or dip on this core section. The geometry of dip direction is shown in Fig. 5. Notably, dip direction is positive in the counterclockwise direction and so describes the angle in degrees west of the orientation line.

   We calculate the dip direction as in Equation (1).

$$\alpha = \tan^{-1}\left(\frac{\tan(\delta_2)}{\tan(\delta_1)}\right). \#(1)$$

5. *Compute dip (δ):* Next we calculate the dip from the horizontal plane as in Equation (2).

$$\delta = tan^{-1}\left(\frac{\tan(\delta_1)}{\cos(\alpha)}\right). \#(2)$$

   As with dip direction, there is a total of 225 dip estimates for an ideal core section.
6. *Assign confidence to dip and dip direction estimates:* The length of the two tracks used to calculate each apparent dip estimate and the maximum Pearson correlation coefficient achieved are recorded. For each estimate of dip and dip direction, we compute a confidence score, which is the product of the length and the correlation coefficient of each pair of tracks. This approach ensures that longer sections of overlap (i.e., longer core sections and adjacent tracks that don't require as much shifting to align) are more heavily weighted. Likewise, pairs of tracks which align well, as indicated by a larger correlation coefficient, are more strongly weighted.
7. *Compute weighted median dip and dip direction:* We find the weighed geometric median of the vectors defined by the dip and dip direction estimates above, calculated numerically with a Weizfeld's algorithm (Wiezfeld, 1937). The use of a median, rather than a mean, ensures a small number of outlying estimates do not impact the central result. Prior to this calculation, dip estimates which are negative are modified to be

https://doi.org/10.1017/jog.2025.10081 Published online by Cambridge University Press

positive, with the dip direction correspondingly adjusted by 180°. The vector describing each pair of dip and dip direction estimates (*v*) is described in Equation (3).

$$v = \begin{pmatrix} \cos\delta \sin\alpha \\ \cos\delta \cos\alpha \\ sin(\delta) \end{pmatrix} \#(3)$$

The Weizfeld's algorithm iteratively minimizes the weighted sum of angular distances (*D*) by refining the median vector (*m*). This equation is shown in Equation (4), where *w* represents the weight assigned to each estimate's vector and N the total number of vectors.

$$D(m) = \sum_{i=1}^{N} w_i \, arccos(\langle v_i, m \rangle) \#(4)$$

Once *m* is found, the median dip direction (α_m) and median dip (δ_m) are described in Equation (5) and Equation (6).

$$\alpha_m = arctan2(m_y, m_x) \#(5)$$

$$\delta_m = \arcsin(m_z) \#(6)$$

8. *Identify uncertain median estimates:* Once this median is calculated, we find the maximum angular radius of a circle centered at the weighted median direction such that 50% of the weight (the interquartile range, or IQR) is contained within this radius. We find that on sections where this circle is greater than 16° in diameter, the spread of estimates is too wide to reliably capture the dip, and so we exclude these sections from analysis. The 16° threshold is successful at excluding sections which do not coalesce to a clear cluster of estimates, while still allowing for some uncertainty due to noise.
Figure 5 somewhere near here.

3. RESULTS

Both ALHIC2201 and ALHIC2302 show clear layering in both AC and DC measurements. The magnitude of variation in conductance and the thickness of the layers varies among sections. Most layering is not observable with visual inspection, although a visible layer of particles in ALHIC2201 results in a clear low in DC conductivity and a clear peak in AC conductivity (Fig. 6), consistent with neutralized acidity and elevated ion content from a tephra layer.
Figure 6 near here.

Confident dip estimates which meet the 16° IQR threshold are achieved on 71% of measured core sections. On 14.5% of measured core sections, there are not three or more pairs of tracks with >20 cm of overlapping ECM. This was largely caused by either small cracks impacting electrode contact in shallow ice, or constrained cut geometry limiting the number of tracks in ALHIC2201 due to the prior sampling on this core. The remaining 14.5% of measured core sections spread the central 50% of estimated weight over more than 16° (and in most cases, much greater). These sections are more homogenous to AC ECM, and so were the most impacted by noise.
Figure 7 near here.

The average dip calculated for ALHIC2201 is 29° with a standard deviation of 5.5°. ALHIC2302 has steeper dips, with an average of 69° and a standard deviation of 3.7°. In Fig. 8, we fit a linear trendline to the median dips over depth and find slopes of -0.56° m^{-1} in ALHIC2201 and -0.18° m^{-1} in ALHIC2302. A t-test indicates statistically significant trends ($p \leq .05$)

https://doi.org/10.1017/jog.2025.10081 Published online by Cambridge University Press

for ALHIC2302 (p=0.003), but not ALHIC2201 (p=.085). This analysis excludes dip estimates where the interquartile range exceeds the 16° threshold.
Figure 8 near here.

The dip can be ~10° offset from an adjacent core section, as seen with variations in the dip shown in Fig. 7 (e.g., near 25 m depth in ALHIC2302). These variations exceed the interquartile range of some pairs of adjacent core sections. This may indicate actual changes in layer orientation at these fine scales, but it may also indicate sources of measurement error not captured in the uncertainty presented in the layer dip estimate. The orientation of the core tray and non-perpendicular face cuts both may be responsible for some degree of error but are unlikely to explain the full spread in the data.

We also present the weighted circular mean for dip direction estimates, as shown in Fig. 9, where the weighted mean of the x and y components of the circular data are individually computed and combined into a final angular average. We do not present percentile results, as we do for dip, due to the ambiguity in presenting percentile/median results on circular datasets. For both cores, the orientation of layering is generally consistent (within ~25°) between depths where the core logs note orientation was lost. We suspect the exceptions to this (e.g. 17-20 m vs. 21-23 m in ALHIC2201 and the spread from 10-20 m in ALHIC2302) may be driven by errors with transferring the orientation line. The significant changes to dip direction where the orientation was lost is expected, as the position of the orientation line relative to the ice stratigraphy may have changed.
Figure 9 near here.

The azimuth of the orientation line was consistent for the upper 17 m of ALHIC2201. Therefore, dip direction estimates from the uppermost sections of this core can be added to the azimuth of the orientation line to determine the dip azimuth. The dip direction of the upper 17 m of ALHIC2201 is on average 220° counterclockwise of the orientation line. This orientation line has a measured azimuth of 56° (clockwise from north) at the surface. Thus, the dip azimuth of this section of ALHIC2201 is 200°. This measurement has significant uncertainty, including +/- 5° on the orientation line GPS azimuth measurement, and a standard deviation of 13° in the dip direction calculations across this measurement range. Determining dip azimuth is not possible on ALHIC2302, as the azimuth of the orientation line was not measured and, even if the azimuth of the orientation line was known at the surface, the orientation was lost above the first 3D ECM dip calculation.

4. DISCUSSION

4.1 Implications for ice core sampling

The combination of steeply dipping layering and large-diameter cores presents new challenges for ice core analysis. In most ice core analysis campaigns, the depth of each sample is carefully measured, but the location of the sample within the core's cross section is not. This is built on the assumption that the layering is near-horizontal, and so multiple measurements at the same depth all sample the same layers. This is not the case in Allan Hills ice. A dip of 70° will result in a single layer having a >0.6 m offset in depth across the width of a large-diameter core. This uncertainty exceeds the sub-centimeter resolution of many modern ice core analysis techniques and complicates the development of multi-proxy records which are assembled from multiple parallel sets of samples.

https://doi.org/10.1017/jog.2025.10081 Published online by Cambridge University Press

The combination of 3D ECM and careful logging of the three-dimensional location of each sample enables parallel sets of measurements to be placed on a common depth scale. We recorded this information for samples from ALHIC2302 in advance of an upcoming multi-institution core sampling campaign. Multiple vertical sticks from different locations within the core will be measured for the same parameters to verify the reproducibility of the measurements. The layering imaged with 3D ECM will allow multi-proxy records from Allan Hills cores to have cm-accurate depth alignment similar to conventional ice cores. Unfortunately, sampling on ALHIC2201 was completed before 3D ECM measurements were made and accurate depth alignment of samples will not be possible in this core.

4.2 Interpretation of layer orientation

Both ALHIC2201 and ALHIC2302 show large dips with a gradual trend towards shallower dip with depth. This relationship meets a $p<0.05$ threshold for ALHIC2302 but is narrowly exceeded for ALHIC2201. The 3D ECM alone is insufficient to generalize for the entire region, and future studies combining 3D ECM with radar surveys will examine if these results are broadly true across the Allan Hills. The 3D ECM results presented here are also restricted to shallow ice, where the core quality is best, and does not directly address the stratigraphic complexities in the oldest and deepest ice.

This characterization of dip with depth provides insight into the larger scale stratigraphy at the core sites. While 3D ECM allows the orientation of the sections to be aligned relative to one another, the lack of azimuth information prevents aligning the sections with other spatial observations without additional constraints. To demonstrate this concept, we have chosen to illustrate two of many potential scenarios consistent with the 3D ECM observations in Fig. 10. Fig. 10a shows bed-parallel layering, due to ice flow up the bedrock feature, with surface ablation potentially steepening the layers near the surface, similar to the affect of scour zones on near surface layering in the interior of the ice sheet (Das and others, 2015). Fig. 10b shows the remaining portion of a fold after the upper part has been removed by ablation; in this scenario, the layers get deeper in the ice flow direction. Both scenarios are consistent with the 3D ECM results and differentiating between them requires additional information.

Figure 10 near here.

Ice-penetrating radar data collected in 2019 (Nesbitt and Brook, 2023) provides additional context for these results. While the mismatch between core depths and the radar identification of the bedrock visualized in Fig. 11 indicate some off-axis reflectors may be introducing error into bedrock depth estimates, the radar data provide useful constraints on the bedrock geometry and englacial layering. A radar track (Track 2) perpendicular to the nearby nunatak, which passes the ALHIC2201 drill site, shows englacial layering in the upper 70 m roughly parallel to the bed topography along this track. The apparent dip of the bedrock below the ice core site in this track (28°) is also similar to the average 3D ECM layer dip in ALHIC2201 (28°).

Notably, the azimuth of dip direction for the upper 17 m of ALHIC2201 is 61° off this radar track, in the direction of the local bedrock dip as interpolated from the radar data (Fig. 11c. This implies the actual bedrock dip may be steeper than dips observed in Track 2 and the 3D ECM data. However, as demonstrated by both ice cores exceeding the bed depth estimate (Fig. 11a and 11b), there is significant uncertainty in bed geometry. The combination of englacial layering and bedrock geometry observed in radar data as well the 3D ECM dip and dip azimuth

https://doi.org/10.1017/jog.2025.10081 Published online by Cambridge University Press

all suggest the englacial stratigraphy in this core is driven by bedrock geometry. Thus, the scenario in Fig. 10a, where layering is parallel with the bed, is well supported for ALHIC2201. Figure 11 near here.

The interpretation of 3D ECM data for ALHIC2302 is less constrained. A radar track roughly perpendicular to the nunatak passes nearby the ALHIC2302 core site, as shown in Fig. 11a. This radar track shows bed slopes at 33° near the core site, which are steep, but significantly less than the 68° dip observed in ECM data. Here, there are no visible englacial layers in the radar data. Therefore, a range of layer geometries, including both conceptual geometries shown in Fig. 10, are possible.

The 3D ECM results presented here also constrain potential folding of englacial layering in both cores. If there were folds with a radius of 5-20 m, we would expect to see 3D ECM dips steadily increasing to vertical, and then decreasing within the ECM datasets in this study. Such changes are not observed, as the changes to dip with depth are gradual. However, there is the potential for folding to still play a role in the layering. For example, a very large fold (as shown in Fig. 10b, with a radius >>20 m, could be consistent with the gradually changing dips in both cores. A small-diameter fold, with a radius on the order of ~1-5 m, might be too small for enough 3D ECM measurements to capture the progressive change in dips through the fold. Even smaller radius folds (<1 m radius) would present as curving layering within a single section of 3D ECM data although we do not observe layer curvature or cm-scale folding in the 3D ECM data.

It is also possible for there to be disruptions to the original layering, even if folding is not resolved in the 3D ECM data. Waddington and others (2001) demonstrate the potential for the formation of recumbent folds to form as a result of “wrinkles” in stratigraphy and simple sheer. The authors note these recumbent folds (as portrayed in Fig. 10a might not result in clear disruptions to stratigraphy, even as they represent significant reversals to ice core chronologies. Indeed, in 3D ECM data a recumbent fold would not be distinguishable from other layering. Identification of these features would require additional ice core sampling and dating methods.

4.3 Potential for azimuthal orientation

Determining the azimuth of ice cores has been a long pursued and elusive goal in ice core science. Microstructure and physical properties studies of ice cores often depend on core azimuth to link ice properties to glacier flow, and vice versa (e.g., Weikusat and others, 2017). Given the significant interest in the glaciological conditions and ice flow necessary for preservation of old ice at the Allan Hills, measurements of ice fabric may provide insight into the current and past ice flow. The fabric information will be more valuable if it can be oriented in space.

The current method for determining ice core azimuth includes aligning the breaks between adjacent core sections to extrapolate a known azimuth down through the core. This method is currently used at the Allan Hills, but core quality limits its utility to the upper meters of the core. Direct azimuth logging during drilling on each core section is difficult to achieve accurately even with modern ice core drilling technology (Fitzpatrick and others, 2014) and is not currently attempted on the large-diameter drill used at the Allan Hills. Recent work by Westhoff and others (2021) presents a novel approach combining borehole inclination and azimuth logging with visual line scanning but requires the assumption of flat layering and that the apparent dips are due to the borehole being not perfectly vertical. Allan Hill ice cores have

https://doi.org/10.1017/jog.2025.10081 Published online by Cambridge University Press

particularly complex layer geometries and challenging core quality such that previous techniques are not applicable.

3D ECM presents a new pathway towards determining ice core azimuth in blue ice areas with complex stratigraphy. With 3D ECM, the dip direction can be determined relative to the core but is not referenced to azimuth. Ground-penetrating radar data can provide the additional information needed to determine ice core azimuth by matching the dip direction from ECM with the dip direction calculated from radar surveys. Because radar data is GPS-referenced, this would enable the determination of the azimuth of the dip direction in Allan Hills cores, and so the orientation of the cores themselves.

This effort will require a dedicated radar campaign, employing a high frequency radar system (~200 MHz) to clearly image layering in the upper 70 meters. Current Allan Hills radar data, collected with 100 MHz antennas, does resolve some layering dipping roughly in line with the bed above ALHIC2201 (Nesbitt and Brook, 2023). However, this data is not sufficient to clearly resolve layer dip. Avoiding spatial aliasing, and consequently enabling accurate migration after data collection, will require sub-meter posting intervals and so very slow collection speeds (Holschuh and others, 2014). A relatively omnidirectional (rather than directional) profiling radar system would ensure that sloping reflectors off the vertical axis are still well resolved. A radar campaign designed to provide perpendicular scans of englacial stratigraphy across the depth range where 3D ECM measurements have been obtained is possible as part of future field work in the Allan Hills.

5. CONCLUSION

Here we present a novel 3D ECM method for imaging layering in ice cores. We compute the apparent dip on two perpendicular faces of an ice core by finding the depth offset between parallel ECM tracks. Combining the apparent dip on both perpendicular faces enables the computation of both dip and dip direction, uniquely defining layer orientations. We use the spread of estimates from each pair of tracks on both faces to constrain the uncertainty.

3D ECM measurements on ALHIC2201 and ALHIC2302 identify consistent and sloping layering in both cores. Radar data supports the interpretation that the layers in ALHIC2201, with a dip of 28°, are likely parallel to local bed geometry. The steeper layering in ALHIC2302 might be driven by the steeper bed topography at this site, although a lack of constraints on englacial layering from radar data means more complex layer orientations cannot be ruled out. Both cores show a gradual trend towards less steeply dipping layering with depth.

We believe future work can improve on the 3D ECM method. A clear priority for future development of the method is devising cut plans which enable two perpendicular sets of ECM measurements, and so 3D ECM, on conventional small diameter ice cores (~100 mm rather than the 241 mm cores in this study). Core quality is generally better in these conventional small diameter cores, which would enable 3D ECM results to provide insight into layering into deeper ice than was possible in this study. Further developments to multitrack ECM methods, like employing >2 electrodes simultaneously (e.g. Wolff et al., 1999), may improve sampling times, although previous attempts have struggled to maintain consistent electrode contact.

3D ECM promises to be useful to a range of future ice core interpretation efforts. Combined with dedicated radar surveys, 3D ECM might enable the determination of the azimuth of each core section, useful in physical properties studies. 3D ECM also will enable

https://doi.org/10.1017/jog.2025.10081 Published online by Cambridge University Press

depth alignment of multiple sets of parallel sampling, where the layer dip would otherwise introduce significant uncertainty of relative depth scales.

DATA AVALIBILITY

3D ECM data from this paper, along with basic plots of all core sections and angle calculations, are available at the US Antarctic Program Data Center (https://doi.org/10.15784/601967). Code can be accessed on Zenodo (https://doi.org/10.5281/zenodo.16879471).

AUTHOR CONTRIBUTION STATEMENT

Kirkpatrick collected all 3D-ECM data, led the analysis, and wrote most of the paper. Fudge assisted in the experiment design, analysis, and paper writing. Shackleton, Marks Peterson, and Carter logged cores in the field and provided notes on the orientation line. All authors contributed to core processing at the National Science Foundation (NSF) Ice Core Facility.

AKNOWLEDGEMENTS

This work was supported by the U.S. National Science Foundation (NSF) Center for Oldest Ice Exploration (NSF COLDEX), an NSF Science and Technology Center (NSF 2019719), and by NSF grant 2149518. We thank the NSF Office of Polar Programs, the NSF Office of Integrative Activities, and Oregon State University for financial and infrastructure support, and the NSF Antarctic Infrastructure and Logistics Program, the NSF Ice Drilling Program, the NSF Ice Core Facility, and the Antarctic Support Contractor for logistical support. We thank the NSF Ice Drilling Program for support activities through NSF Cooperative Agreement 1836328.

In addition to the named authors, we appreciate the contributions of additional members of the 2022-2023 Allan Hills field team (Science Team: Jacob Morgan, Peter Neff, Yuzhen Yan. Drillers: Elizabeth Morton, Michael Jayred. Support Staff: Johnathan Hayden.) and the 2023-2024 Allan Hills field team (Science Team: Abigail Hudak, Asmita Banerjee, Edward Brook, John Higgins, John-Morgan Manos. Drillers: Elizabeth Morton, Michael Jayred. Support Staff: Ashley Goverman, Emalia Mayo.). We also thank NSF COLDEX project members who contributed the 2023 and 2024 COLDEX Core Processing Lines and Jacob Chalif for editing assistance.

COMPETING INTERESTS

The authors declare none.

https://doi.org/10.1017/jog.2025.10081 Published online by Cambridge University Press

REFERENCES

Alley RB, Gow AJ, Meese DA, Fitzpatrick JJ, Waddington ED and Bolzan JF (1997) Grain-scale processes, folding, and stratigraphic disturbance in the GISP2 ice core. *Journal of Geophysical Research: Oceans* **102**(C12), 26819–26830. doi:10.1029/96JC03836.

Bender ML, Barnett B, Dreyfus G, Jouzel J and Porcelli D (2008) The contemporary degassing rate of 40Ar from the solid Earth. *Proceedings of the National Academy of Sciences* **105**(24), 8232–8237. doi:10.1073/pnas.0711679105.

Bindschadler R and others (2008) The Landsat Image Mosaic of Antarctica. *Remote Sensing of Environment* **112**(12), 4214–4226. doi:10.1016/j.rse.2008.07.006.

Das I, Scambos TA, Koenig LS, van den Broeke MR and Lenaerts JTM (2015) Extreme wind-ice interaction over Recovery Ice Stream, East Antarctica. *Geophysical Research Letters* **42**(19), 8064–8071. doi:10.1002/2015GL065544.

Faria SH, Freitag J and Kipfstuhl S (2010) Polar ice structure and the integrity of ice-core paleoclimate records. *Quaternary Science Reviews* **29**(1), 338–351. doi:10.1016/j.quascirev.2009.10.016.

Fischer H and others (2013) Where to find 1.5 million yr old ice for the IPICS 'Oldest-Ice' ice core. *Climate of the Past* **9**(6), 2489–2505. doi:10.5194/cp-9-2489-2013.

Fitzpatrick JJ and others (2014) Physical properties of the WAIS Divide ice core. *Journal of Glaciology* **60**(224), 1181–1198. doi:10.3189/2014JoG14J100.

Fudge TJ, Taylor KC, Waddington ED, Fitzpatrick JJ and Conway H (2016) Electrical stratigraphy of the WAIS Divide ice core: Identification of centimeter-scale irregular layering. *Journal of Geophysical Research: Earth Surface* **121**(7), 1218–1229. doi:10.1002/2016JF003845.

Hammer CU (1980) Acidity of Polar Ice Cores in Relation to Absolute Dating, Past Volcanism, and Radio–Echoes. *Journal of Glaciology* **25**(93), 359–372. doi:10.3189/S0022143000015227.

Higgins JA and others (2015) Atmospheric composition 1 million years ago from blue ice in the Allan Hills, Antarctica. *Proceedings of the National Academy of Sciences* **112**(22), 6887–6891. doi:10.1073/pnas.1420232112.

Holschuh N, Christianson K and Anandakrishnan S (2014) Power loss in dipping internal reflectors, imaged using ice-penetrating radar. *Annals of Glaciology* **55**(67), 49–56. doi:10.3189/2014AoG67A005.

Jansen D and others (2016) Small-scale disturbances in the stratigraphy of the NEEM ice core: observations and numerical model simulations. *The Cryosphere* **10**(1), 359–370. doi:10.5194/tc-10-359-2016.

https://doi.org/10.1017/jog.2025.10081 Published online by Cambridge University Press

Karlsson NB and others (2018) Glaciological characteristics in the Dome Fuji region and new assessment for "Oldest Ice". *The Cryosphere* **12**(7), 2413–2424. doi:10.5194/tc-12-2413-2018.

Kuhl TW, Johnson JA, Shturmakov AJ, Goetz JJ, Gibson CJ and Lebar DA (2014) A new large-diameter ice-core drill: the Blue Ice Drill. *Annals of Glaciology* **55**(68), 1–6. doi:10.3189/2014AoG68A009.

Meese DA and others (1997) The Greenland Ice Sheet Project 2 depth-age scale: Methods and results. *Journal of Geophysical Research: Oceans* **102**(C12), 26411–26423. doi:10.1029/97JC00269.

Mojtabavi S and others (2020) A first chronology for the East Greenland Ice-core Project (EGRIP) over the Holocene and last glacial termination. *Climate of the Past* **16**(6), 2359–2380. doi:10.5194/cp-16-2359-2020.

Moore JC and Paren JG (1987) A New Technique for Dielectric Logging of Antarctic Ice Cores. *Le Journal de Physique Colloques* **48**(C1), C1-155-C1-160. doi:10.1051/jphyscol:1987123.

Nesbitt I and Brook E (2023) I-165-M GPR Field Report 2019-2020. doi:10.15784/601669.

Rasmussen SO and others (2013) A first chronology for the North Greenland Eemian Ice Drilling (NEEM) ice core. *Climate of the Past* **9**(6), 2713–2730. doi:10.5194/cp-9-2713-2013.

Rasmussen SO and others (2006) A new Greenland ice core chronology for the last glacial termination. *Journal of Geophysical Research: Atmospheres* **111**(D6), D06102. doi:10.1029/2005JD006079.

Severi M, Udisti R, Becagli S, Stenni B and Traversi R (2012) Volcanic synchronisation of the EPICA-DC and TALDICE ice cores for the last 42 kyr BP. *Climate of the Past* **8**(2), 509–517. doi:10.5194/cp-8-509-2012.

Spaulding NE and others (2012) Ice motion and mass balance at the Allan Hills blue-ice area, Antarctica, with implications for paleoclimate reconstructions. *Journal of Glaciology* **58**(208), 399–406. doi:10.3189/2012JoG11J176.

Spaulding NE and others (2013) Climate archives from 90 to 250 ka in horizontal and vertical ice cores from the Allan Hills Blue Ice Area, Antarctica. *Quaternary Research* **80**(3), 562–574. doi:10.1016/j.yqres.2013.07.004.

Sugiyama K and others (2000) Measurement of electrical conductance in ice cores by AC-ECM method. *Physics of Ice Core Records,* ed. T. Hondoh, 173-184. Hokkaido University Press, Sapporo, Japan, http://hdl.handle.net/2115/32468"

Svensson A and others (2005) Visual stratigraphy of the North Greenland Ice Core Project (NorthGRIP) ice core during the last glacial period. *Journal of Geophysical Research: Atmospheres* **110**(D2), D2108. doi:10.1029/2004JD005134.

https://doi.org/10.1017/jog.2025.10081 Published online by Cambridge University Press

Takata M, Iizuka Y, Hondoh T, Fujita S, Fujii Y and Shoji H (2004) Stratigraphic analysis of Dome Fuji Antarctic ice core using an optical scanner. *Annals of Glaciology* **39**, 467–472. doi:10.3189/172756404781813899.

Taylor KC and others (2004) Dating the Siple Dome (Antarctica) ice core by manual and computer interpretation of annual layering. *Journal of Glaciology* **50**(170), 453–461. doi:10.3189/172756504781829864.

Taylor KC, Alley RB, Lamorey GW and Mayewski P (1997) Electrical measurements on the Greenland Ice Sheet Project 2 Core. *Journal of Geophysical Research: Oceans* **102**(C12), 26511–26517. doi:10.1029/96JC02500.

Taylor KC and others (1993) Electrical conductivity measurements from the GISP2 and GRIP Greenland ice cores. *Nature* **366**(6455), 549–552. doi:10.1038/366549a0.

Taylor KC and Alley RB (2004) Two-dimensional electrical stratigraphy of the Siple Dome (Antarctica) ice core. *Journal of Glaciology* **50**(169), 231–235. doi:10.3189/172756504781830033.

Waddington ED, Bolzan JF and Alley RB (2001) Potential for stratigraphic folding near ice-sheet centers. *Journal of Glaciology* **47**(159), 639–648. doi:10.3189/172756501781831756.

WAIS Divide Project Members (2013) Onset of deglacial warming in West Antarctica driven by local orbital forcing. *Nature* **500**(7463), 440–444. doi:10.1038/nature12376.

Weikusat I and others (2017) Physical analysis of an Antarctic ice core—towards an integration of micro- and macrodynamics of polar ice*. *Philosophical Transactions of the Royal Society A: Mathematical, Physical and Engineering Sciences* **375**(2086), 20150347. doi:10.1098/rsta.2015.0347.

Weiszfeld, E (1937) Sur le point pour lequel la somme des distances de n points donnés est minimum. *Tohoku Mathematical Journal, First Series **43***, 355-386.

Westhoff J and others (2021) A stratigraphy-based method for reconstructing ice core orientation. *Annals of Glaciology* **62**(85–86), 191–202. doi:10.1017/aog.2020.76.

Wilhelms F (2005) Explaining the dielectric properties of firn as a density-and-conductivity mixed permittivity (DECOMP). *Geophysical Research Letters* **32**(16), L16501. doi:10.1029/2005GL022808.

Wilhelms F, Kipfstuhl J, Miller H, Heinloth K and Firestone J (1998) Precise dielectric profiling of ice cores: a new device with improved guarding and its theory. *Journal of Glaciology* **44**(146), 171–174. doi:10.3189/S002214300000246X.

Wolff E, Brook E, Dahl-Jensen D, Fujii Y, Lipenkov VY and Severinghaus J (2006) White paper: The oldest ice core: A 1.5 million year record of climate and greenhouse gases from

https://doi.org/10.1017/jog.2025.10081 Published online by Cambridge University Press

Antarctica. https://icedrill.org/library/white-paper-oldest-ice-core-15-million-year-record-climate-and-greenhouse-gases-antarctica.

Wolff E (2000) Electrical stratigraphy of polar ice cores : principles, methods, and findings. *Physics of Ice Core Record*s, ed. T. Hondoh, 155-171. Hokkaido University Press, Sapporo, Japan, http://hdl.handle.net/2115/32467

Wolff E, Basile I, Petit J-R and Schwander J (1999) Comparison of Holocene electrical records from Dome C and Vostok, Antarctica. *Annals of Glaciology* **29**, 89–93. doi:10.3189/172756499781820888.

Yan Y and others (2019) Two-million-year-old snapshots of atmospheric gases from Antarctic ice. *Nature* **574**(7780), 663–666. doi:10.1038/s41586-019-1692-3.

FIGURE CAPTIONS

Figure 1. Location of ALHIC2302 and ALHIC2201 in the Allan Hills blue ice area. Figure uses Landsat Image Mosaic of Antarctica data (Bindschadler and others, 2008) for a true-color representation of the region. Grid north is up, and true north is indicated by the arrow. Selected ice flow trajectory data from Spaulding and Others (2012) is shown with the red arrows, where the direction of the arrow indicates the flow direction, and the size labels represents the flow speed. Ice flow trajectories from the ice core sites themselves are not currently available.

Figure 2. (a) A section of ice from ALHIC2302 being scanned for electrical conductivity. The DC electrodes are pressed against the ice surface, measuring a single track (in this case, track 2), while the AC electrodes are hidden behind them. This section of ice is rotated 90° counterclockwise around the depth-axis relative to its orientation in reference diagrams in (b) and (d), to enable measurement of the “left” face. (b) and (c) show a cross section, where depth increases out of the page, of the cut from both ALHIC2302 and ALHIC2201 large-diameter cores. A cross section of the smaller, standard 4” core is shown for scale. The “top,” “left,” and “right” ECM face nomenclature is also shown. (d) A three-dimensional representation of ALHIC2302 depicting the six AC- and DC-ECM tracks.

Figure 3. Two core sections of ALHIC2302 AC 3D ECM data from 25.1 to 26.9 m in depth with strong ECM layering. Depth increases to the bottom left. The diagram shows both faces of a quarter-core cut, with the white gap representing the short gap between sections which could not be measured with 3D ECM. Note the well-defined and steeply dipping layering.

Figure 4. (a) ECM data from a 1 m section of ALHIC2302. Each line represents a single track, with the shading indicating distance across the core. (b) Same data in top-down view, as with Fig. 2, with the color bar indicating the electrical current. (c) Zoom in of the feature highlighted by the box in (a), showing the depth of tracks 1 and 6 before and after shifting to the angle of maximum correlation between the two tracks. (d) Relationship between the correlation coefficients between pairs of tracks and the test angle, with the tracks 1 and 6 correlation coefficient in red.

Figure 5. Diagram demonstrates the principal behind the calculation of the three-dimensional layer orientation. The purple and orange shaded planes represent the two measured faces, and gray shaded plane represents the true dip plane. Here δ_1 and δ_2 represent the apparent dip in two perpendicular planes, and δ represents the dip. α represents the angle between the vertical

https://doi.org/10.1017/jog.2025.10081 Published online by Cambridge University Press

plane aligned with the core's orientation line and the plane of dip. Given that δ_1 and δ_2 are in perpendicular planes, α and δ can both be calculated as a function of δ_1 and δ_2.

Figure 6. AC and DC ECM data from ALHIC2201 section 19_1. Plots show depth increasing down the y-axis. The x-axis represents distance from center of core, measured from the corner where the two perpendicular faces ("right" and "top") meet. The color bar for AC and DC shown at the bottom of the figure is held consistent on both faces. The outermost tracks (which occasionally have a reduced amplitude than inner tracks, likely due to reduced thickness at the edge of the sample) are normalized to match the average value of other tracks for visual clarity. The strong layering at 16.15 (highlighted by the black box) is coincident with a faint band of dark particles, but this was only noticed after the reduced DC conductivity and elevated AC conductivity was noted. This layer, and others in the section, are visibly dipping in both planes. Sections with poor electrode contact are marked in black.

Figure 7. Section dips from ALHIC2201 (a) and ALHIC2302 (b). Individual dip estimates are denoted by dots, where the size is proportional to the confidence score. The weighted median dip for each section is shown with a blue bar. Sections which exceed the 16° IQR threshold are shown in grey instead of black. Sections where no dip estimate was achieved are shown with red dashed lines.

Figure 8. Fitting a trendline to the median dips shows moderate trends with dip, which meet a $p<0.05$ significance threshold for ALHIC2302 but not ALHIC2201. The dip changes by -0.56 and -0.16° per m on ALHIC2201 (a) and ALHIC2302 (b) respectively. Sections which exceed the 16° IQR threshold are shown with grey dots, and not used for the line fit.

Figure 9. The weighted circular average dip direction is plotted against depth for each section in ALHIC2201 (a) and ALHIC2302 (b). Note that the average dip direction estimate is generally consistent where drill logs indicate continuous core orientation. Lost orientation is indicated by the horizontal black dashed lines. Sections where the estimate exceeds the 16° IQR threshold are shown in grey, and sections where the dip cannot be calculated are shown with a red dashed line. Here the calculated dip direction has been rotated by 180° for sections where the median dip is negative.

Figure 10. A conceptual sketch depicts two potential layering scenarios in an Allan Hills setting which might produce 3D ECM results consistent with decreasing dips with depth. A wider array of scenarios is possible, but these two provide a useful demonstration of the range of potential layering configurations. In 10a (left), layering is largely driven by bed topography. A recumbent fold is included to demonstrate how consistent layer orientation does not guarantee stratigraphic order. In this scenario, layering dips more steeply near the surface, potentially driven by surface ablation. In an alternative scenario 10b (right), a fold driven by a past flow regime is partially ablated away, resulting in steeply dipping layering. 3D ECM alone cannot conclusively differentiate between these two scenarios.

Figure 11. (a) and (b) Bed picks from radar tracks (Nesbit and Brook, 2023) roughly perpendicular to the outcrop at the ALHIC2302 and ALHIC2201 sites. A representation of the ALHIC2302 and ALHIC2201 is included, showing their total depth and noting their distance from the radar track. The average ECM layer orientations from this study are shown in red and the 40-meter average bed slope for each core is shown in green. This visualization should not be regarded as exact, as there are no observational constraints on ALHIC2302 dip azimuth and, even where constrained, the ALHIC2201 dip azimuth is 61° off the radar track (although the bed

https://doi.org/10.1017/jog.2025.10081 Published online by Cambridge University Press

slope appears similar in both directions). (c) Interpolated radar bed depths (Nesbitt and Brook, 2023), with the locations of the ALHIC2201 and ALHIC2302 core sites noted. The dip direction azimuth for the upper section of ALHIC2201 is shown with the red arrow. While not parallel to the radar line, it does dip with the local bed topography. As with Fig. 1, this plot is oriented with grid north up, and the arrow indicates true north.

Figure 1

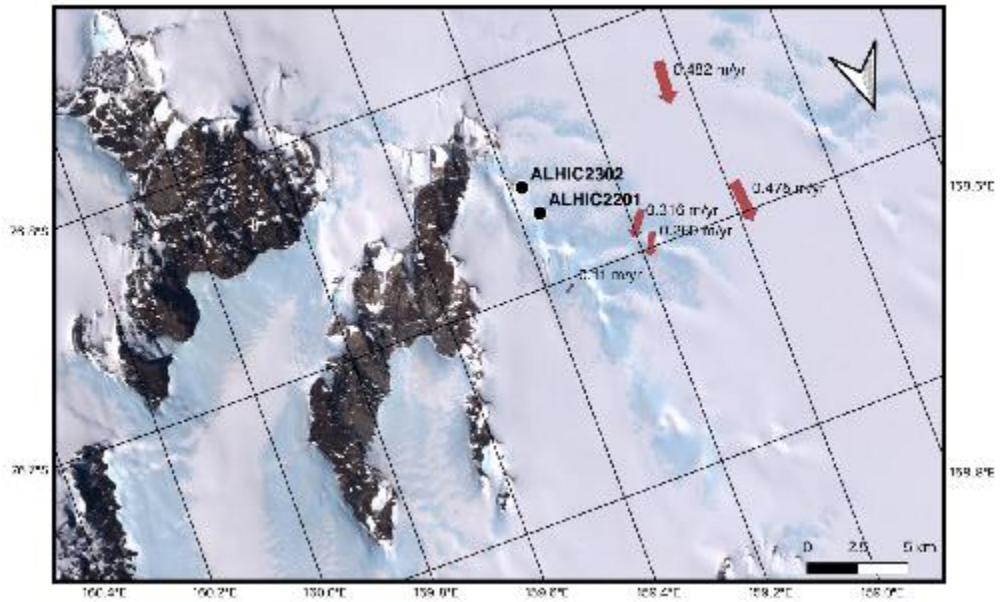

https://doi.org/10.1017/jog.2025.10081 Published online by Cambridge University Press

Figure 2

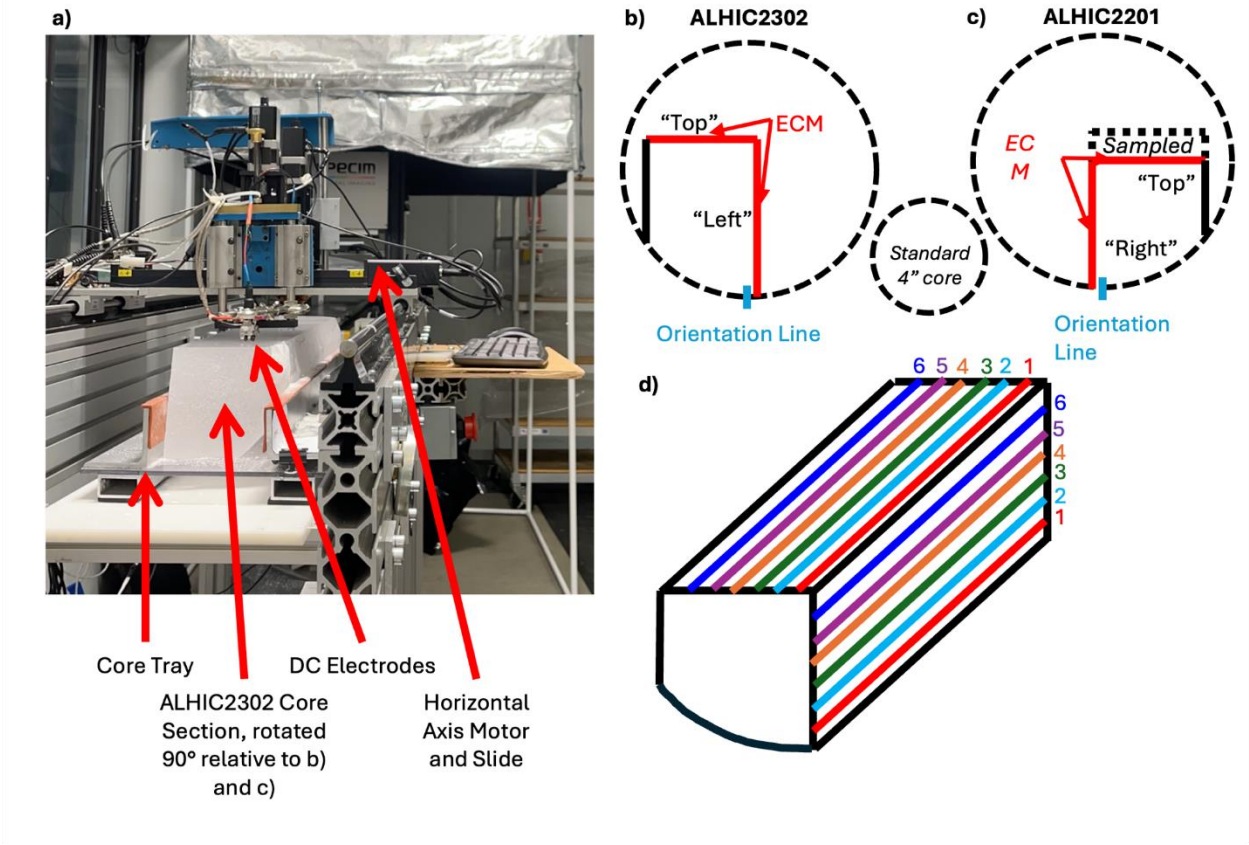

https://doi.org/10.1017/jog.2025.10081 Published online by Cambridge University Press

Figure 3

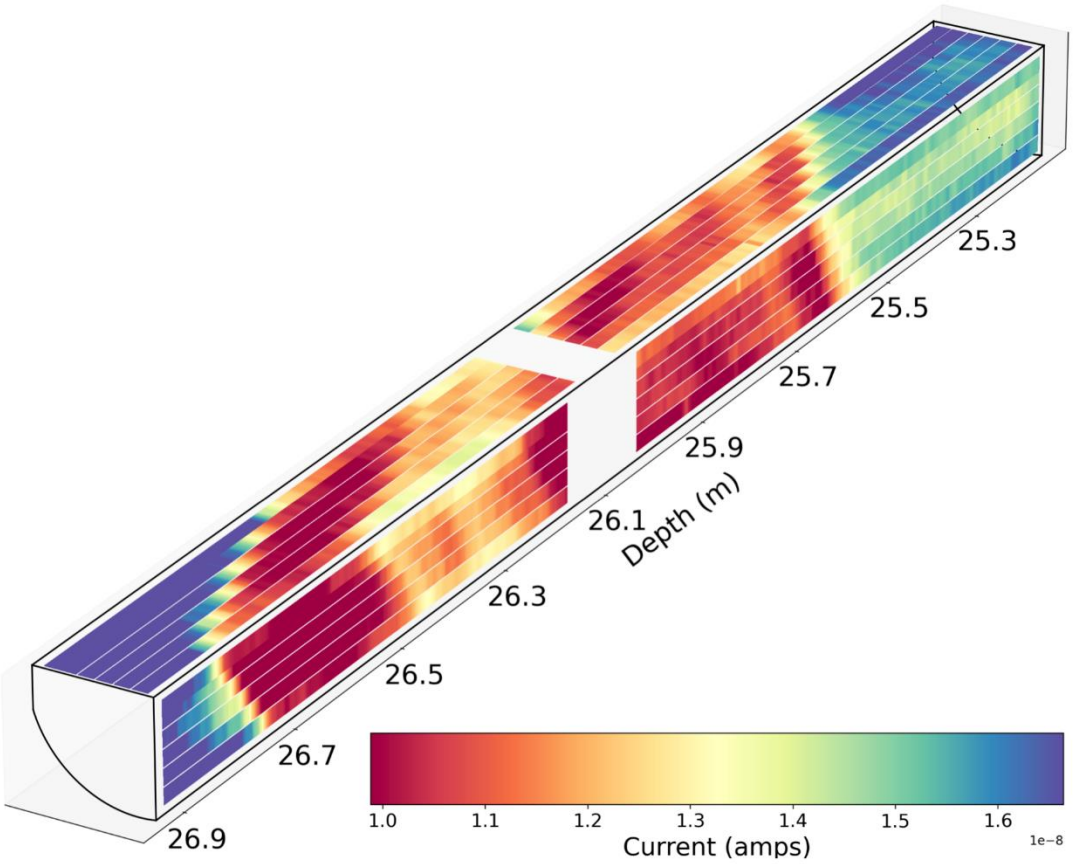

https://doi.org/10.1017/jog.2025.10081 Published online by Cambridge University Press

Figure 4

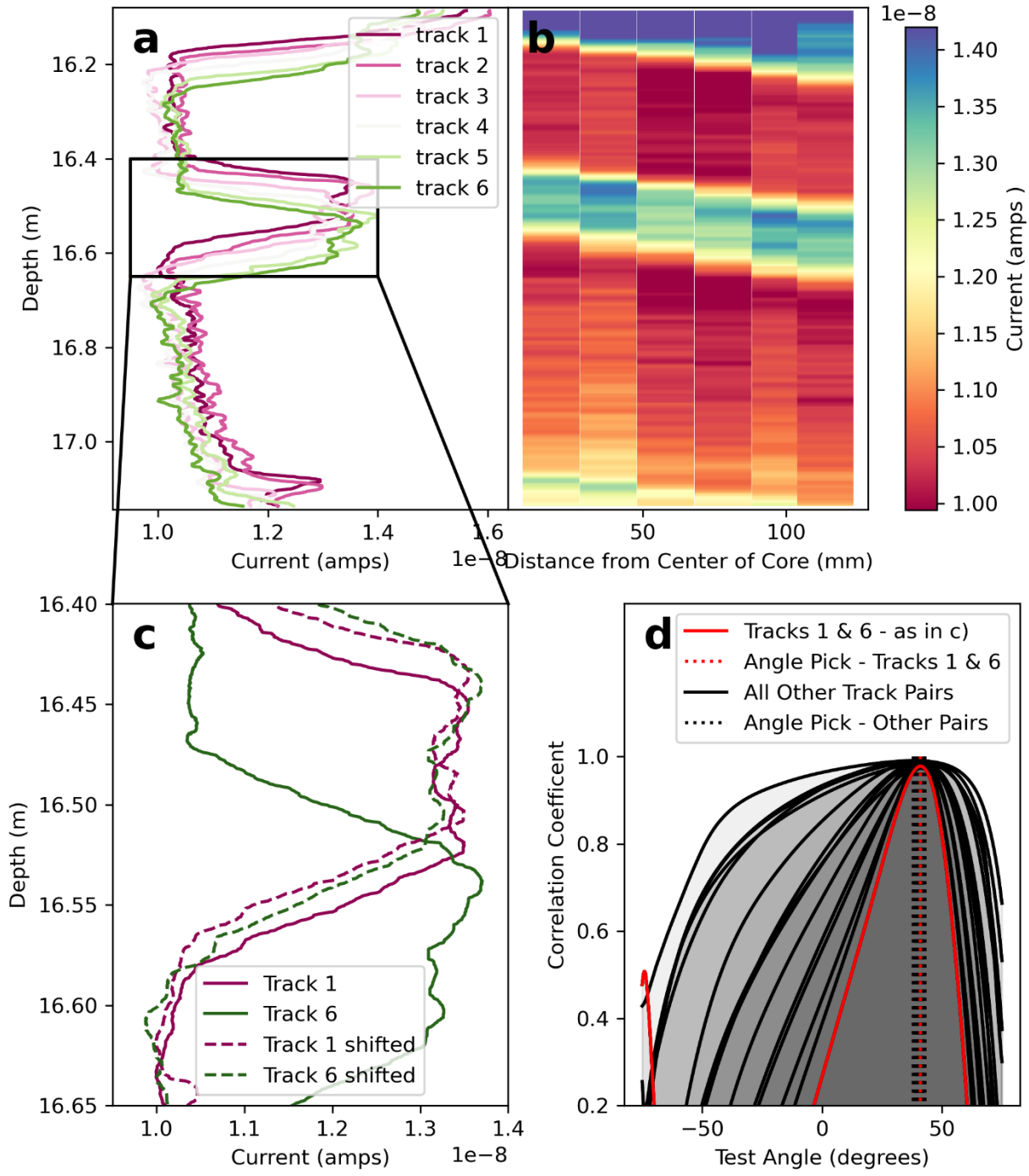

https://doi.org/10.1017/jog.2025.10081 Published online by Cambridge University Press

Figure 5

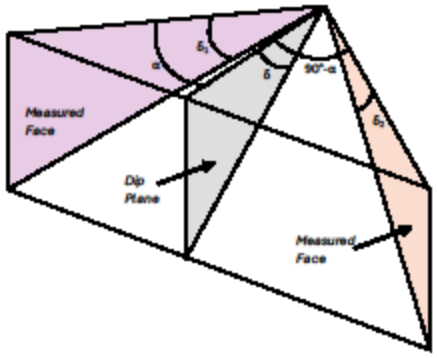

Figure 6

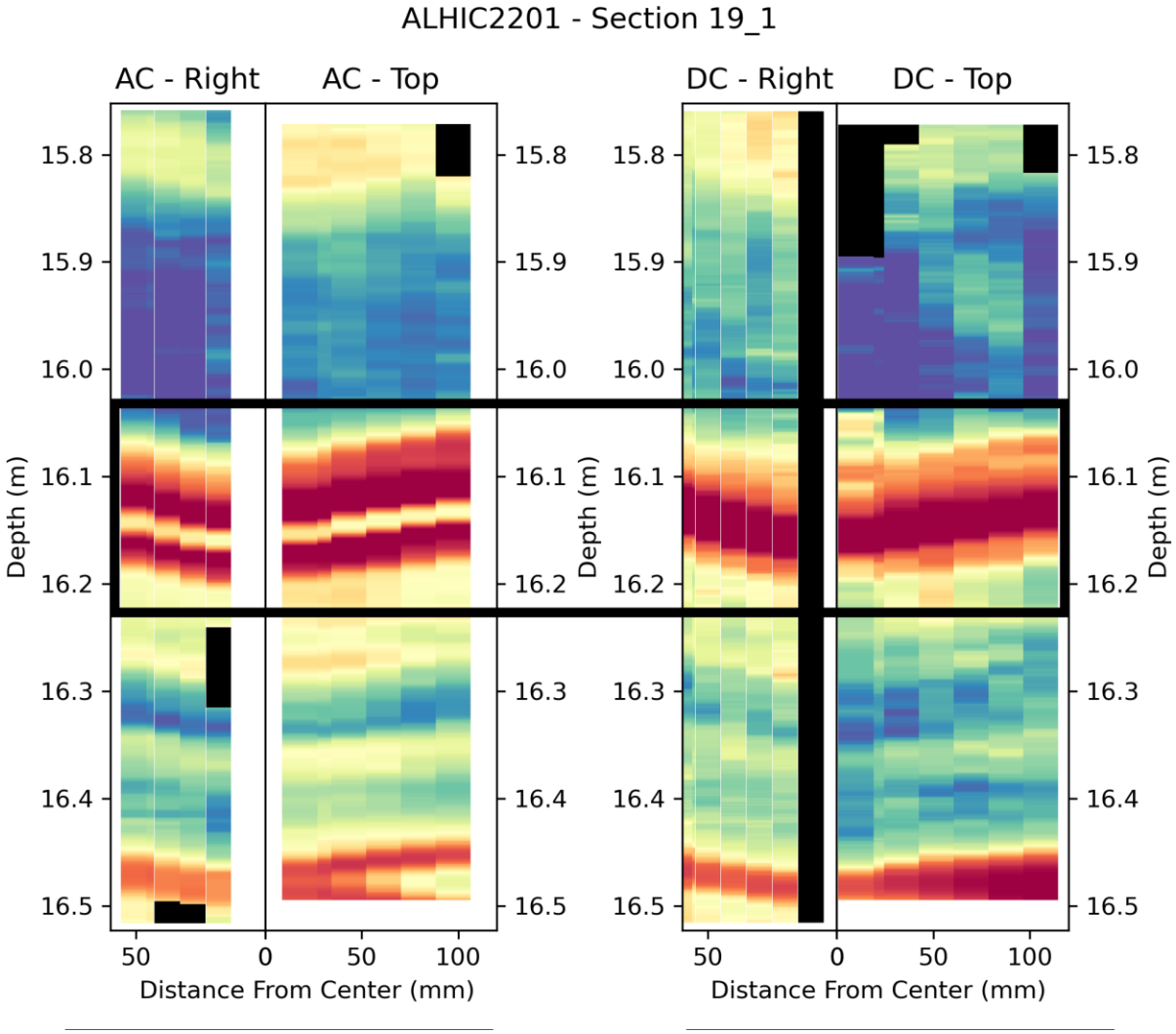

https://doi.org/10.1017/jog.2025.10081 Published online by Cambridge University Press

Figure 7

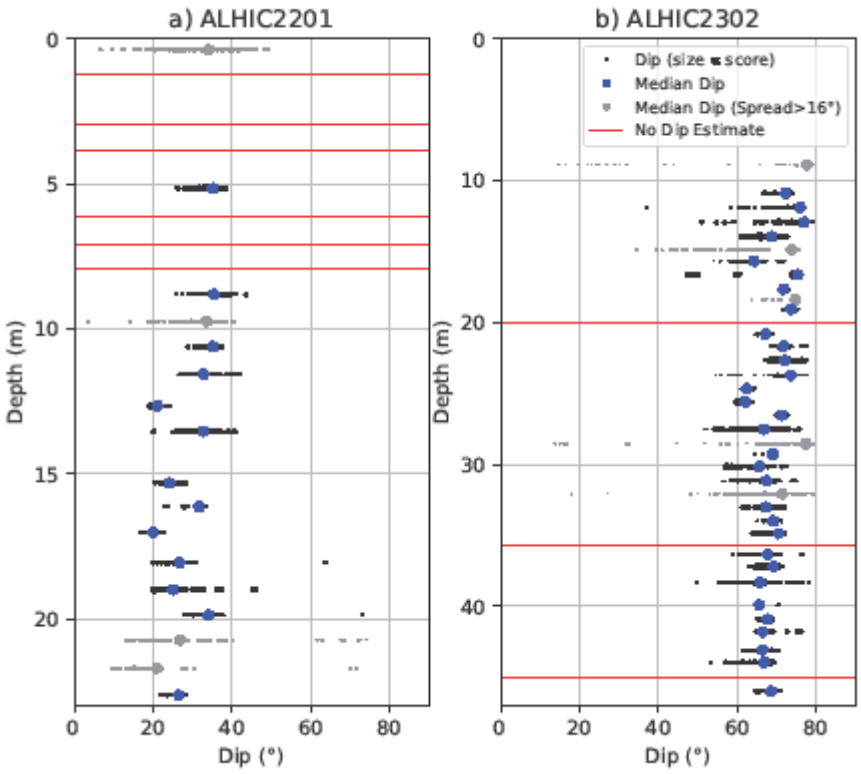

https://doi.org/10.1017/jog.2025.10081 Published online by Cambridge University Press

Figure 8

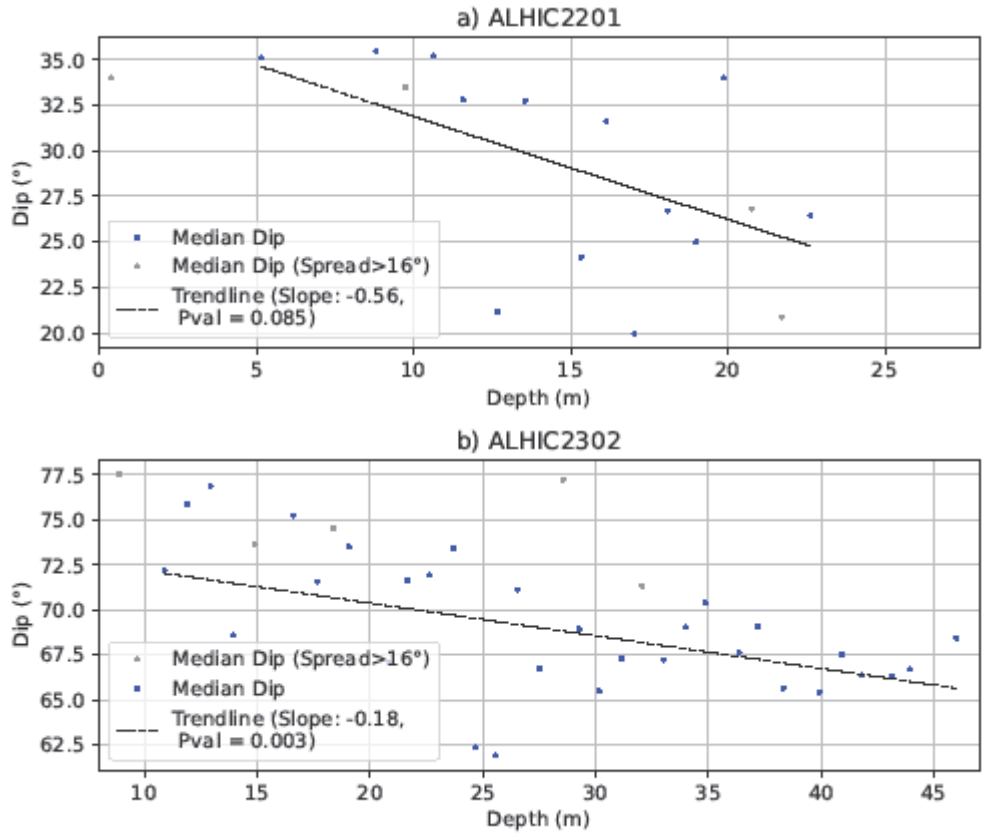

https://doi.org/10.1017/jog.2025.10081 Published online by Cambridge University Press

Figure 9

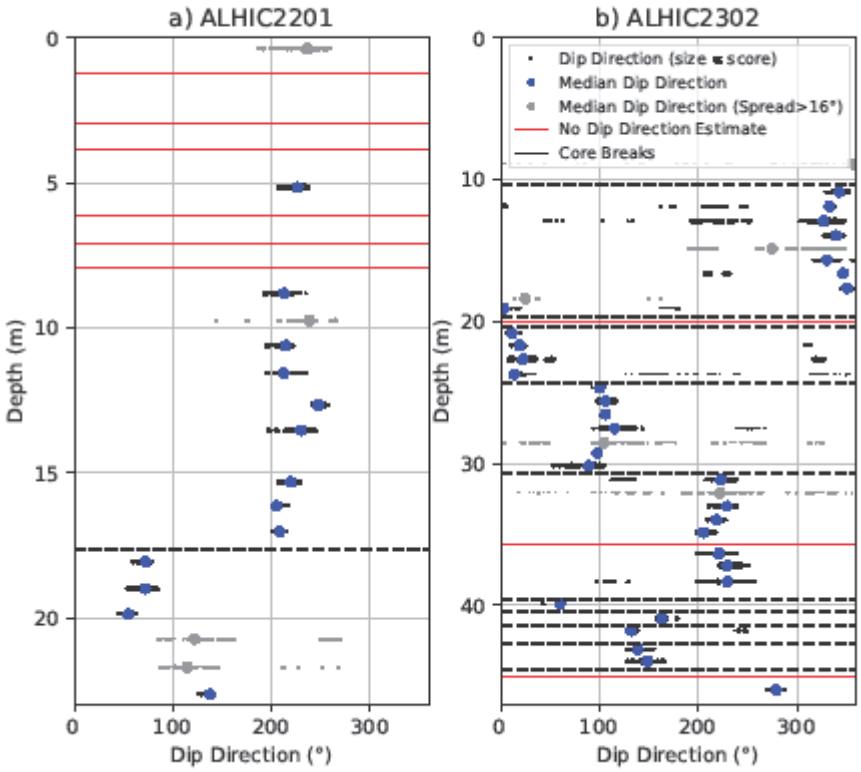

https://doi.org/10.1017/jog.2025.10081 Published online by Cambridge University Press

Figure 10

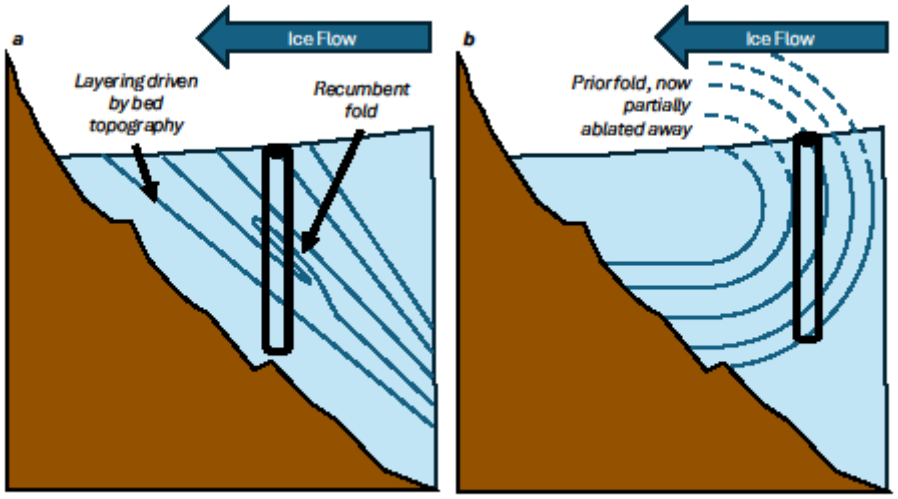

Figure 11

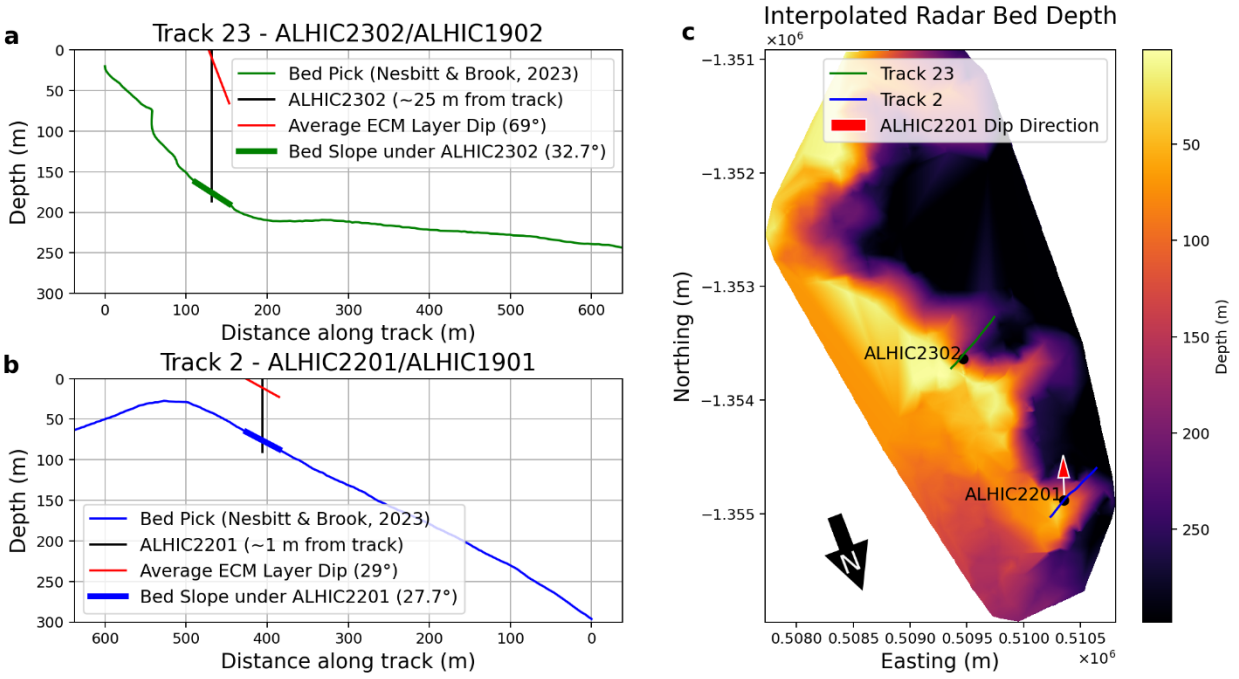

https://doi.org/10.1017/jog.2025.10081 Published online by Cambridge University Press